LANGMUIR

pubs.acs.org/Langmuir Article

Crystallization Control of Anionic Thiacalixarenes on Silicon Surface Coated with Cationic Poly(ethyleneimine)

Anna A. Botnar, Oleg P. Novikov, Oleg A. Korepanov, Ekaterina A. Muraveva, Dmitry A. Kozodaev, Alexander S. Novikov, Michael Nosonovsky, Ekaterina V. Skorb,* and Anton A. Muravev*

Cite This: https://doi.org/10.1021/acs.langmuir.4c03488 Read Online

ACCESS | Metrics & More | Article Recommendations | Supporting Information

ABSTRACT: Surface modification of solid substrates with organic molecules and polyelectrolytes is a promising strategy toward advanced soft materials due to the control of molecular arrangement and supramolecular organization; however, understanding the nature of interactions within the assembly is challenging. Here a facile approach to the control of the architecture of calixarene macrocycles on soft surfaces is presented through the interplay of weak interactions involving a solid silicon substrate, a cationic polyelectrolyte layer, and anionic sulfonatothiacalix[4]arene (STCA). Topological analysis of atomic force microscopy (AFM) images of STCA on silicon, as well as silicon wafers modified with neutral polyethylenimine (PEI) and cationic PEI-H$^+$, indicates different surface morphology and assembly behavior of STCA on such substrates. Drop-casting a calixarene solution onto silicon induces the formation of chaotically oriented needle crystals. When there is globular PEI, a nucleation point for the STCA crystals is formed on the polyelectrolyte surface, which grows into rosette structures. In contrast, protonated PEI with a chain-like structure alters the self-organization of STCA on silicon surfaces, leading to a dense uniform fiber-like network. Density functional theory modeling of the system components' self-assembly reveals thermodynamically favorable face-to-face antiparallel aggregation of STCA monomers and contribution of H-bonding into PEI(PEI-H$^+$)−STCA and Si−STCA association.

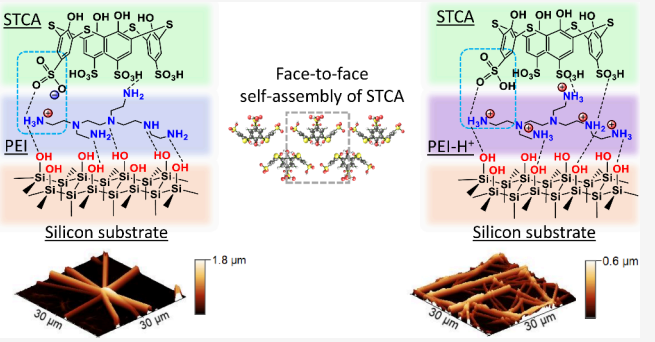

INTRODUCTION

Polyelectrolytes play a key role in the development of soft materials for optical and electronic,[1−3] sensor,[4−6] and biomedical applications.[7−12] These polymers are attractive due to the formation of a coacervate phase displaying a confined medium, which is easily formed via a layer-by-layer strategy.[13−16] An interesting development of polyelectrolyte-based functional coatings emerged from the incorporation of multivalent cavitands, such as calixarene scaffolds.[17−19] These nontoxic molecules offer a nanosized cavity suitable for encapsulation or surface recognition of multiple guest molecules, from organic dyes[20] and drugs[21] to proteins[22] and nucleotides.[23] Calixarenes are easily tunable due to the presence of upper- and lower-rim functionalities, which widely exploit the cooperativity behavior of guest binding.[24] An additional control factor of binding by calixarenes could be the compartmentalization of host−guest complexation, e.g., phospholipid membrane[25] or air−water interface.[26−28] All of these components add much complexity to the construction of a digital computational model, which could reliably predict not only the self-organization of macrocycles on soft surfaces but also the target characteristics of the derived functional materials. At present, there are many works related to the density functional theory (DFT) evaluation of the molecular forces stabilizing the polymer−organic molecule,[29] substrate−organic molecule,[30] and substrate−polymer assemblies (Figure 1).[31,32]

Visualization of self-organization phenomena involving macrocycles and polymer structures requires nanoscale characterization techniques along with advanced topology analysis tools. Atomic force microscopy (AFM) is a convenient method for the morphological and nanomechanical characterization of nanomaterials with a wide range of surface roughness, thickness, adhesion, elasticity, stiffness, and other parameters. Topological analysis of AFM images employing modern mathematical algorithms (Voronoi diagram construction, binarization, segmentation, noise reduction, contrast enhancement, Vietoris−Rips complex generation, etc.) and machine learning algorithms (including those from Python libraries) that extract semantic information (Voronoi entropy, porosity, and

Received: September 5, 2024
Revised: October 20, 2024
Accepted: November 4, 2024

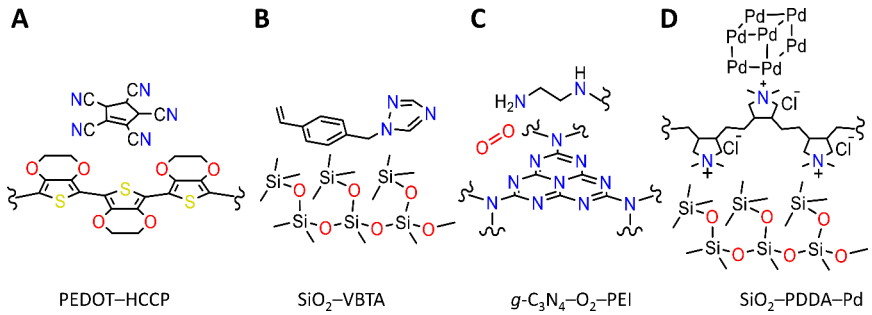

Figure 1. Examples of DFT evaluation of the interaction energy values between substrate and polymer models and inorganic and small organic molecules. (A) Model of oligo(3,4-ethylenedioxythiophene) and heptacyanocyclopentenide (polymer–organic molecule interaction).[29] (B) Model of 1-(4-vinylbenzyl)-1*H*-1,2,4-triazole on glass (SiO_2) surface (substrate–organic molecule interaction).[30] (C) PEI oligomer adsorbed on g-C_3N_4 with O_2 (substrate–polymer interaction).[31] (D) Model of SiO_2, poly(diallyldimethylammonium chloride) and Pd crystal.[32]

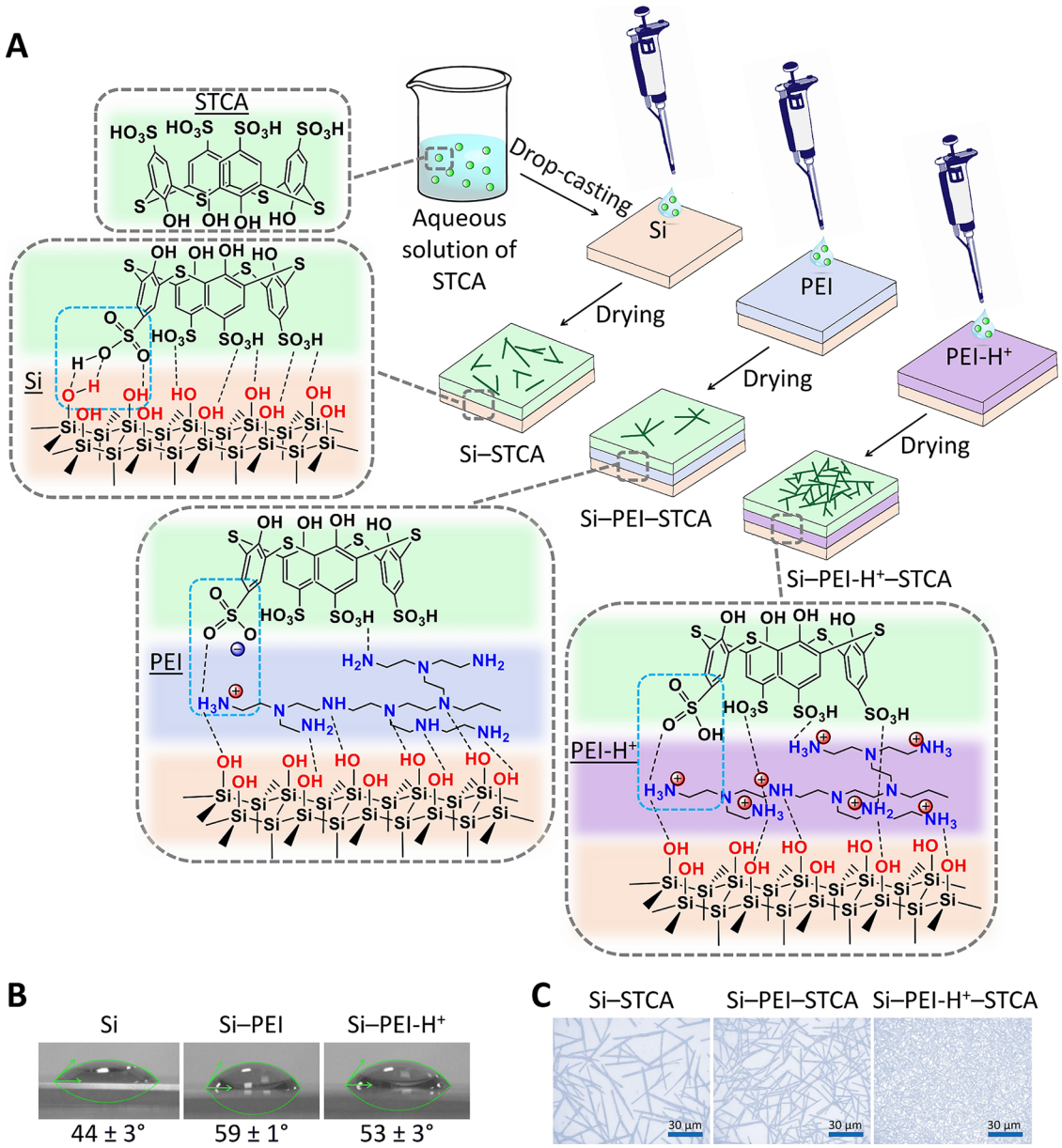

Figure 2. Fabrication of STCA films on modified silicon surfaces. (A) Scheme of crystallization of STCA on the Si surface, as well as the layer of PEI and PEI-H^+ on the Si wafer, including possible molecular interactions. (B) Contact angle images for water droplets on Si, Si–PEI, and Si–PEI-H^+ surface. (C) Optical microscope images of the films (scale bar is 30 μm).

https://doi.org/10.1021/acs.langmuir.4c03488
Langmuir XXXX, XXX, XXX–XXX

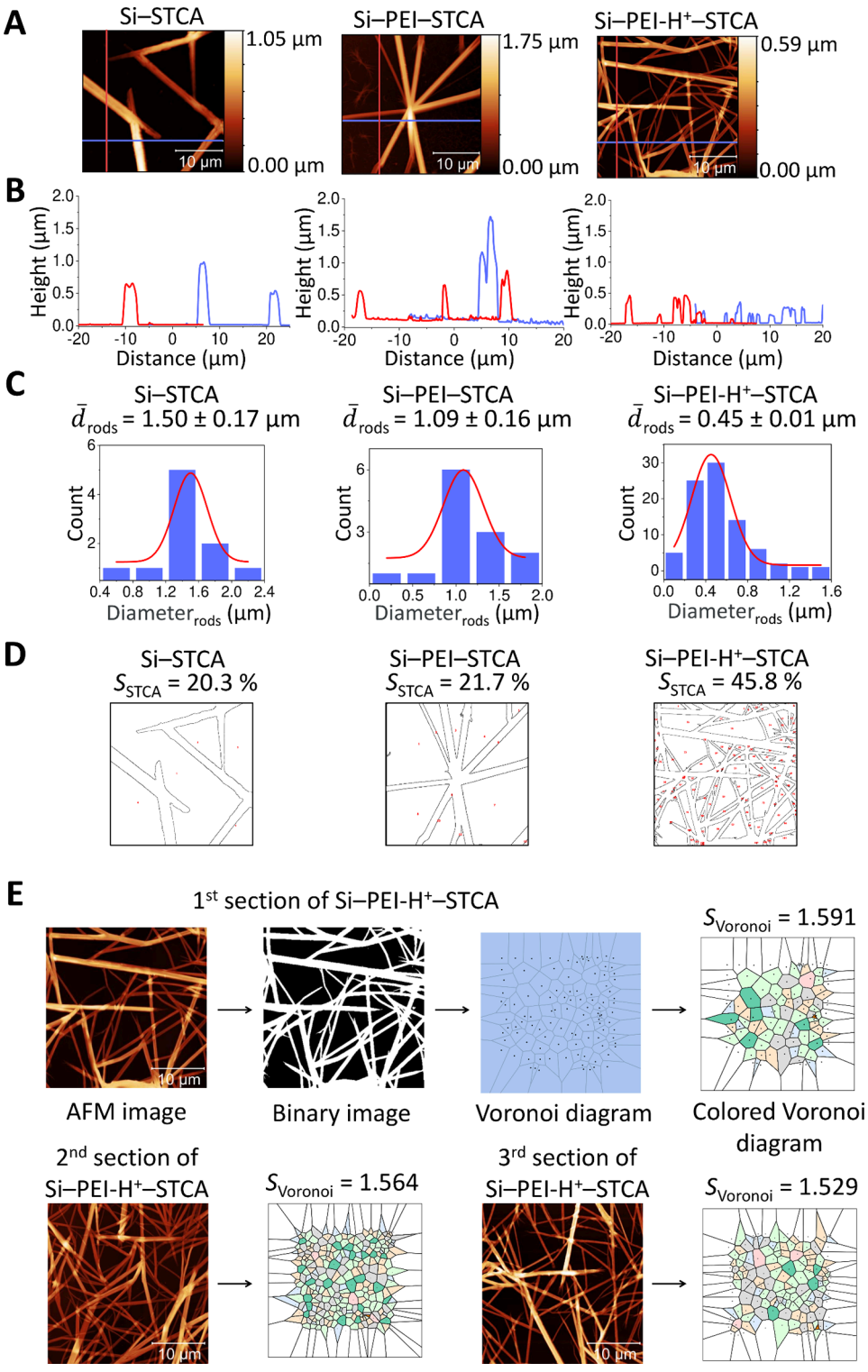

Figure 3. Topological data analysis of AFM images. (A) AFM topography images of STCA crystals on a silicon wafer (Si–STCA) and on polyelectrolyte coating (Si–PEI–STCA, Si–PEI-H$^+$–STCA) (scan size is 30 × 30 μm; scale bar is 10 μm). (B) Horizontal (blue) and vertical (red) height profiles that are taken along the lines shown in panel A. (C) Diameter distribution histograms of STCA rods with superimposed best-fitting curves. (D) Grayscale AFM images with segmented calixarene fibers for the calculation of the surface coverage of STCA rods (regions indicated by red points correspond to voids). (E) Algorithm of the Voronoi entropy calculation using AFM images of Si–PEI-H$^+$–STCA.

particle size distribution) adds a new dimension to the evaluation of nanostructural features.[33−36]

Here we utilize the STCA–PEI–Si hybrid inorganic–organic assembly to probe the self-assembly behavior of macrocyclic scaffolds on soft surfaces to further add recommendations for the design of tailored materials in the fields of biomedicine, surface engineering, and shaping of ionic and molecular flows for information processing.

https://doi.org/10.1021/acs.langmuir.4c03488
Langmuir XXXX, XXX, XXX−XXX

RESULTS

Fabrication of STCA Films. Calixarene-containing films on different substrates were prepared according to dip coating and drop casting techniques, as illustrated in Figure 2a. As indicated by atomic force microscopy, the Si substrate had an atomically smooth surface (the surface roughness is ca. 0.4 nm) after hydrophilization with piranha solution (Figure S1a,b). An increase in hydrophilicity of the substrate due to the formation of multiple silanol groups was confirmed by sessile drop water contact angle measurements (44 ± 3° on piranha-washed Si (Figure 2b) vs 60 ± 2° on untreated one (Figure S1a, inset)). Subsequent dip coating of Si wafer into PEI-containing solutions and drying overnight afforded a smooth surface with the mean square roughness value of ca. 0.5 nm (Figure S1c). Deposition of more hydrophobic PEI onto the Si wafer increased the mean square roughness by up to 0.6 nm (Figure S 1d) and the contact angle up to 59 ± 1° (Figure 2b). It should be noted that PEI exists in aqueous solutions as a weak base with pH 9 and forms a globular structure stabilized by multiple hydrogen bonds,[37] which is highlighted in the AFM image. With a decrease in pH, amino groups of PEI are protonated, intramolecular hydrogen bonds are partially broken, and the macromolecule adopts chain conformation.[37] In this case, the PEI-H^+ polymer forms hydrogen bonds between the oxygen atoms of the silanol groups of the wafer and the hydrogen atoms of PEI. Contact angle measurements confirm an increase in surface hydrophilicity as compared to PEI-coated wafer (53 ± 3 vs 59 ± 1°).

STCA was transferred onto the polyelectrolyte-modified or Si surface via a drop-casting technique from a 10^{-3} mol L^{-1} aqueous solution. Optical microscopy observation of the evaporation of the aqueous solution of STCA revealed the crystallization of macrocycle in the form of fibers (Figure 2c), the distribution density of which slightly varied going from Si wafer to the PEI- and PEI-H^+-coated substrate. When the solution of STCA is deposited onto a hydrophilic silicon surface, chaotically arranged needle-like crystals are formed, whereas the presence of PEI induces the formation of rosettes made from needle crystals growing from the nucleation point on the wafer surface presumably due to the globular structure of PEI. Notably, the Si−PEI-H^+−STCA assembly appeared as densely distributed fibers of calixarene. These preliminary data suggest a strong dependence of the adhesion strength and crystallization behavior of STCA molecules on the hydrophilicity of the substrate.

AFM Image Analysis and Nanomechanical Characterization of the Coatings. The height distribution of the STCA crystals provided by AFM imaging (Figure 3a) indicated that STCA crystals deposited onto the PEI coating are larger (ca. 1.8 μm in maximum height) than those on the silicon surface (ca. 1 μm) due to the layering caused by the presence of nucleation points of STCA represented by PEI. In contrast, the rods of calixarene on the PEI-H^+ surface provided 3 times smaller crystal height (ca. 0.6 μm) presumably due to the increase in adhesion of STCA to the positively charged polyelectrolyte surface, which agrees with the observation of optical microscope images of drop-cast calixarene solutions (Figure 2c). Moreover, the STCA crystals appear as needles when deposited from a Si wafer and neutral PEI coating, whereas the charged PEI coating directs the crystallization of STCA into fiber-like structures, as indicated by the curved shape of STCA rods.

To establish the dependence of nanomechanical characteristics of STCA rods on the type of coating, Young's modulus (E) and stiffness (k) values were calculated from the force−distance curves upon contact of the cantilever tip with the STCA rods (Figure S2, Table S1). Despite the change in the shape of STCA rods from needles to fibers, Young's modulus and stiffness values varied in a narrow range (E = 28−29 MPa, k = 10−11 $N{\cdot}m^{-1}$) (Table S2), which falls within the range for soft materials.[38] It is difficult to compare the STCA-coated specimens to other organic materials though because the exact values of Young's modulus and stiffness obtained by the AFM technique are controversial and provide only an estimate of the order of magnitude.[39] One reason is that the tip apex is not an ideal sphere, and the scanning surface is not flat. Another reason is that the AFM probe tip generates tip−surface shear forces during cantilever deflection and torsion (lateral and buckling movement), which are not considered in simple models of interaction between the cantilever and surface such as the Hertz model.

The height profiles of the AFM topographical images of the samples (Figure 3b) suggest that there is a more uniform size distribution of STCA crystals. Because of the possible interference of overlapping needles of STCA on the distribution analysis from height profiles, the mean diameter values of STCA fibers were calculated and represented by size distribution histograms (Figure 2c). In this case, the superimposed best-fitting curve followed the unimodal Gaussian distribution, and the mean cross-section sizes of the STCA rods corresponded to 1.5, 1.1, and 0.5 μm for Si−STCA, Si−PEI−STCA, and Si−PEI-H^+−STCA, respectively. The dispersity analysis of the normal distribution curves (Figure 3c) shows a progressive increase in the size uniformity of STCA crystals with a transition from Si wafer to PEI and PEI-H^+ coating with a dispersity value up to 0.03. STCA represents a significantly larger area compared to Si−STCA and Si−PEI−STCA. Another feature of STCA crystals quantified by AFM topological analysis is consistent with the optical microscope images (Figure 2c) and highlights a drastic increase in the surface coverage going from the Si wafer and neutral PEI to the charged polyelectrolyte surface from 20−22 to 46% (Figure 3d). Normalization of the surface coverage by the mean cross-section size of the STCA rods reveals an even larger difference between the coatings of STCA on Si or neutral PEI and charged PEI providing the surface coverage-to-rod diameter ratios of 0.14, 0.20, and 2.02 μm^{-1}, respectively.

An increase in the surface coverage and uniform size distribution of Si−PEI-H^+−STCA coating makes it interesting to evaluate the degree of ordering of the entire assembly using the Voronoi entropy parameter.[40] This was made by generating a Voronoi tessellation from the centroids of the pores enclosed by calixarene fibers (Figure 3e), which is based on the principle that the points in each polygon are the closest to the starting point of that polygon and is defined by the sum of the fractions of polygons with different numbers of sides.[41] The Voronoi entropy value calculated from the three AFM images of Si−PEI-H^+−STCA coating is $S_{Voronoi}$ = 1.561 ± 0.025, while mean $S_{Voronoi}$ values extracted from the optical images of Si−STCA and Si−PEI−STCA (Figure S3) corresponded to 1.888 and 1.753, which are close to that describing random distribution (1.710[41]).

DFT Calculations. To rationalize the formation of linear crystals of STCA on modified and unmodified Si substrates, the thermodynamic favorability of the self-assembly of STCA macrocycles was evaluated theoretically by optimizing geometries of possible dimers with face-to-face and side-to-side orientations of STCA monomers (Figure 4a). The STCA

https://doi.org/10.1021/acs.langmuir.4c03488
Langmuir XXXX, XXX, XXX−XXX

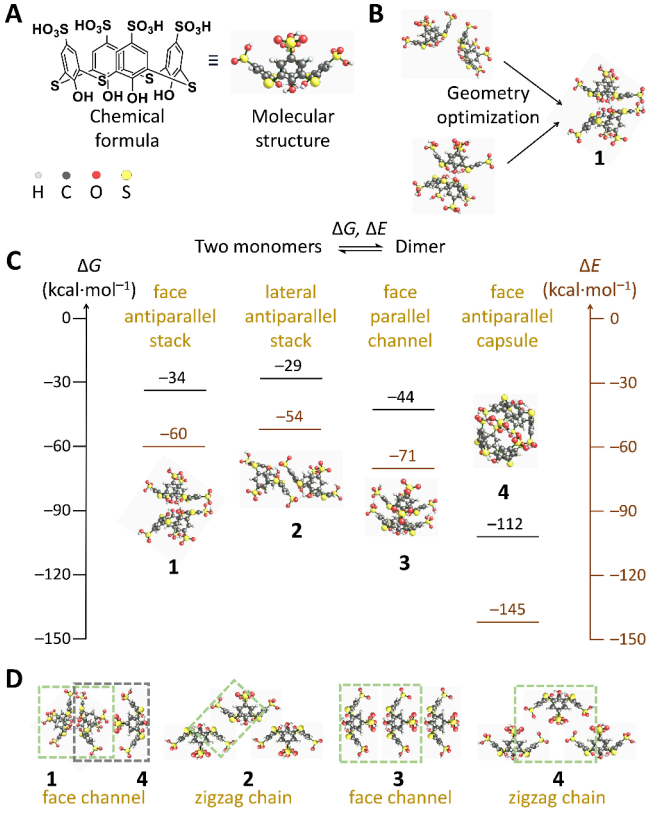

Figure 4. Plausible packing arrangement of STCA in crystals based on DFT models of its dimers. (A) Chemical formula and molecular structure of STCA. (B) Self-sorting behavior of STCA monomers within face-to-face and laterally oriented dimers. (C) Gibbs free energy ΔG (left scale) and total electronic energy ΔE (right scale) profiles of STCA dimerization (B3LYP-D3/def2-SVP level of theory). (D) Possible packing mode of STCA dimers **1**−**4**. H, C, O, and S atoms correspond to white, gray, blue, red, and yellow spheres.

monomer exists in the *cone* conformation in both solution and solid state as evidenced by the NMR spectroscopy (Figures S4 and S5) and supported by crystallographic data from the literature.[42] Previous theoretical works on STCA molecules considered the acid form of STCA instead of sodium salt forms,[43,44] which pose a question of the significance of sodium ion on the assembly process. DFT calculations revealed an intriguing self-sorting behavior of the dimer with face-to-face oriented lower-rim hydroxyl groups and the dimer with laterally oriented STCA monomers, with a parallel arrangement of benzene rings (Figure 4b). These conformers transformed during optimization steps into the geometry of dimer **1**, which is stabilized by both $\pi-\pi$ stacking interactions between two benzene rings and two H-bonds involving SO_3H groups and gives $\Delta G = -34$ kcal·mol^{-1} (Video S1). Meanwhile, the forced formation of intermolecular H-bond in the dimer with face-to-face oriented lower-rim OH groups resulted in the immediate breaking of that bond and zero overall stabilization (Video S2). The antiparallel arrangement of benzene rings at the side-to-side orientation of STCA monomers (dimer 2) also slightly stabilizes the self-assembly by $\Delta G = -29$ kcal·mol^{-1}. Further stabilization of dimer self-assembly could be achieved in face aggregate **3**, with noncentrosymmetric orientation of STCA scaffolds, in which four intermolecular H-bonds are formed. The largest stabilization ($\Delta G = -112$ kcal·mol^{-1}) was calculated for the face antiparallel capsule dimer **4** featuring eight intermolecular −H···O hydrogen bonds between sulfonate groups of the STCA scaffold. It should be noted that the overall trend in the energy profile is the same in cases of both Gibbs free energy ΔG and total electronic energy ΔE (Figure 4c), indicating a comparable contribution of translational, rotational, vibrational, and entropic terms of all dimers into the ΔG value.

Thus, four possible one-dimensional packing modes made from STCA dimers can be hypothesized from DFT calculations: two types of face channel (from dimers **1** and **4**, as well as from dimer **3**) and two types of zigzag chain (from dimers **2** and **4**) (Figure 4d). The zigzag chain made from dimer **4** seems to be predominant in the crystal, which agrees well with the crystal structure of sodium salt and inclusion complexes of STCA.[42,45,46] This finding supports that there is a similar trend of the role of sodium ion in the assembly process of STCA

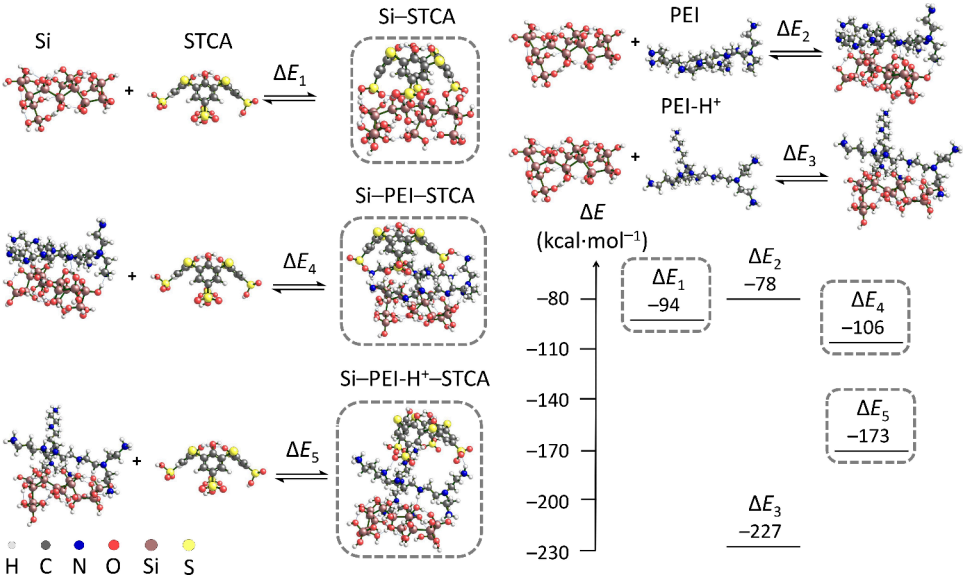

Figure 5. Binding energy ΔE profiles of association among the silanol network, STCA, and PEI (B3LYP-D3/def2-SVP level of theory). The atoms of H, C, N, O, Si, and S are represented by white, gray, blue, red, brown, and yellow spheres, respectively.

https://doi.org/10.1021/acs.langmuir.4c03488
Langmuir XXXX, XXX, XXX−XXX

and validates the choice of the acid form of STCA instead of sodium salt for DFT calculations of dimerization.

Quantum chemical calculations were further carried out for the assemblies involving Si, polyethylenimine, and thiacalixarene. Regarding the competitive role of sodium ion in the STCA molecule in this assembly process, the X-ray structures of inclusion complexes of sulfonatothiacalx[4]arenes with charged molecules do not contain sodium atoms in the unit cell.[47] These literature data illustrate the absence of the direct involvement of sodium in STCA on the assembly process with charged guest molecules and make it reasonable to use the acidic form of STCA for DFT calculations with the charged PEI polyelectrolyte.

Calculation of dimer assemblies **1**−**4** indicates that there is no overall stabilization at close contact of phenolic hydroxyl groups due to the thermodynamically unfavorable cleavage of strong circular intramolecular H-bonding that fixes the cone conformation of STCA. Therefore, only the geometries with close contact between sulfonate groups and polyethylenimine or silicon wafers were considered. The Si wafer was represented by the molecular model possessing covalent Si−Si and Si−OH bonds, as well as O−H···O hydrogen bonds. To represent the neutral and charged branched PEI fragment, a tridecameric model was constructed. In the case of charged PEI, positive charges were assigned to primary and secondary nitrogen atoms by adding hydrogen atoms. To ensure that STCA and polyethylenimine are retained on the silicon wafer, the total electronic energy values of corresponding assemblies (Si−STCA, Si−PEI, and Si−PEI-H^+) were calculated and compared to those of individual components (Figure 5). At this stage, there was always overall stabilization providing large negative ΔE values comparable to those of calixarene dimers (ΔE from −54 to −145 kcal·mol^{-1}, Figure 4c). It should be noted that, despite the formation of stiff STCA fibers on Si wafer, the Si−STCA system is stabilized nearly equally as compared to the Si−neutral PEI assembly (−95 vs −78 kcal·mol^{-1}). This fact is due to the formation of multiple −H···O hydrogen bonds between silanol groups in the former case and O−H···N hydrogen bonds in the latter case. A much larger stabilization evolves in a more branched PEI−H^+−Si system (−227 kcal·mol^{-1}), with multiple N−H···O contacts and electrostatic attraction between O atom and positively charged N atom. Moreover, the PEI-H^+ oligomer significantly expanded during optimization, which provided a larger contact area with the silanol surface and, consequently, a higher adhesion to the model of the Si wafer.

Regarding three-component assemblies, there could be an interplay between hydrogen bonding in the STCA−PEI system and electrostatic interactions between STCA and PEI-H^+ polyelectrolyte. As expected, molecular interactions arising between STCA and polyethylenimine did not alter the adhesion of the polymer to the silanol surface. Bringing STCA into contact with neutral PEI resulted in the proton transfer from one SO_3H group to the nitrogen atom of the primary amino group, with an overall stabilization of ΔE = −106 kcal·mol^{-1}, whereas no proton transfer from other sulfonate groups was observed at subsequent optimization steps. Substitution of PEI-H^+ for PEI in a Si−polyelectrolyte−STCA assembly increased the binding energy up to ΔE = −173 kcal·mol^{-1}, which highlights the increasing role of electrostatic contacts between STCA and PEI-H^+ in preferable interaction with the charged polyelectrolyte surface rather than a neutral one.

The above results suggest that with a transition from the hard Si wafer, on which STCA seems to crystallize with a face-to-face arrangement of sulfonate groups like in dimer **4**, to the neutral and cationic PEI soft material, the lateral antiparallel stacking with a face-to-face-orientation of hydroxyl groups like in dimer **2** becomes preferable. This hypothesis is supported by the decrease in the fiber cross-sectional diameter in Si−PEI(PEI-H^+)−STCA assemblies as compared to Si−STCA (Figure 3c). A decrease in the spacing value from ca. 11.5 Å in the zigzag chain of dimers **4** to 10.8 Å in the zigzag chain of dimers **2** could also contribute to the decrease in the rod diameter. More specifically, despite a small change in the molecular level arrangement of STCA (0.7 Å), the rods and fibers of STCA appear to consist of a large number of stacked zigzag chains (in analogy to the packing of STCA crystals[42]). Therefore, a large number of stacked zigzag chains can lead to such a drastic decrease in the cross section of the rods/fibers from 1.5 to 0.5 μm. Moreover, the increasing role of electrostatic contacts between STCA and PEI-H^+ in preferable interaction with the charged polyelectrolyte surface rather than the neutral one highlights a surface charge neutralization, which results in the decrease in the height of STCA rods. Finally, the transition from straight needles to more curved fibers of STCA crystals with the change of the coating from neutral to positively charged PEI can also be attributed to the weaker interaction between stacked aryl rings in a zigzag chain from dimer **2** rather than a hydrogen-bond network in the zigzag chain made from dimer **4**.

CONCLUSIONS

The combination of dip-coating and drop-casting approaches has afforded rod-shaped crystals of STCA on polyelectrolyte-modified surfaces. The topological data analysis of AFM images has indicated the formation of STCA crystals with a more uniform size distribution (dispersity value decreases from 0.14 to 0.03) going from the silicon wafer to the PEI-coated surface. These results are promising for the development of ion-permeable biocompatible membranes suitable for tissue regeneration and other self-healing materials utilizing the guest encapsulation behavior of the thiacalixarene cavity and adaptive and responsive properties of flexible polyelectrolyte nanofilms. A DFT model of layer-by-layer aggregation of the STCA cavitand on a positively charged or neutral PEI polyelectrolyte on a silanol inorganic network has been elaborated within the B3LYP-D3/def2-SVP level of theory to reveal favorable multiple hydrogen-bonding interactions. Theoretical calculations have also established that STCA molecules tend to dimerize through π-stacking and H-bonding interactions with zigzag chain formation. This allows one to control the architecture of calixarene macrocycles on soft surfaces as presented through the interplay of weak interactions involving the silanol network, cationic polyelectrolyte layer, and anionic STCA.

MATERIALS AND METHODS

Materials. Branched polyethylenimine (PEI, MW = 7.5 × 10^5 g·mol^{-1}), 50 wt % in H_2O (Sigma-Aldrich, St. Louis, United States), and 6 mol·L^{-1} HCl (chemically pure) (LenReactiv, St. Petersburg, Russia) were used as received. The silicon substrate (Flyuorit, St. Petersburg, Russia) was washed consequently with acetone and ethanol, further hydrophilized with piranha solution (3:1 vol % H_2SO_4/H_2O_2), and washed with deionized water (resistivity of 18.2 MΩ·cm). Sulfonatothiacalix[4]arene (STCA) in the form of sodium salt was synthesized according to the literature procedure,[48] and its purity was confirmed by ^{1}H and ^{13}C NMR spectroscopy (Figures S4 and S5).

Surface Modification of Silicon Substrates with STCA and PEI. PEI-modified Si substrates were obtained by dip-coating the substrate in a 2 mg·mL^{-1} PEI aqueous solution with pH 9 (in the case of

https://doi.org/10.1021/acs.langmuir.4c03488
Langmuir XXXX, XXX, XXX−XXX

unprotonated PEI) or pH 3 (in the case of protonated PEI, PEI-H^+), conditioning for 5 min, and washing with deionized water. The pH values of polyelectrolyte solutions were controlled by adding HCl and monitored using a universal indicator paper. The STCA layer was deposited onto the modified or unmodified Si substrate by drop-casting of 30 μL of 10^{-3} mol·L^{-1} aqueous solution of STCA (0.03 μmol) with a Hamilton microsyringe. Each deposition step was followed by drying in a dust-free air atmosphere at room temperature for at least 12 h.

Surface Characterization. The surface topography of the samples was inspected using an AMDSP USB 5 M CMOS microscope camera (China) with a 1/2.5 in. 5 MP image sensor at a 6× zoom, and the selected region was further scanned with an NTEGRA atomic force microscope (NT-MDT BV, Apeldoorn, The Netherlands) in tapping mode at room temperature. Scanning was performed with NSG10 silicon probes having a typical resonant frequency of 240 kHz, force constant of 11.8 N·m^{-1}, and tip radius of 10 nm. The STCA-containing samples gave a coffee-ring effect and, hence, were scanned at the regions far from the edge of the cast drop to ensure reliable and reproducible measurements. The Gwyddion 2.62 program[49] was used to visualize AFM topology and build 1D height−distance vertical and horizontal profiles.

Nanomechanical characteristics of the STCA crystals were determined according to the established protocols[50] from the force−distance curves measured at specific points in contact mode using HQ:CS37/Al BS (MikroMasch, Wetzlar, Germany) silicon probes having a typical resonant frequency of 40 kHz, force constant values of 0.8 N·m^{-1}, tip radius of 8 nm, and full cone angle of 40°. The stiffness of the crystals was calculated as the mean ± RMSD of the slopes of 20 forward force−distance curves. Young's modulus of the crystals at the contact point was calculated within the Hertz fit model using the Nova SPM 1.2 program at specified parameters and a probe force constant of 0.75 N·m^{-1} determined from the force−distance curve measured in a control experiment involving the Si probe and unmodified Si substrate.

Contact angles were determined using the equilibrium profiles of 13 μL water droplets on the modified and unmodified Si substrate (acquired in macro mode with a Mightex SME-C050-U color CMOS camera (Toronto, Canada) at a 10× zoom), which were converted to the 8-bit grayscale color model, using the ImageJ 1.54h program[51] with an LB-ADSA drop analysis plugin by manual adjustment of the position and shape of the green oval shown in Figure 2B to the borders of the drop.

Topological Analysis of AFM Images with STCA. Quadratic mean R_q and arithmetic mean surface roughness R_a were calculated as follows:

$$R_a = \frac{1}{N}\sum_{j=1}^{N}|r_j| \tag{1}$$

$$R_q = \sqrt{\frac{1}{N}\sum_{j=1}^{N} r_j^2}, \text{ where} r_j = z_j - \overline{z} \tag{2}$$

where z_j is the height of the surface profile along the x axis and $\overline{z}$ is the mean value of the height of the surface profile.

The polydispersity (σ) of fiber diameter values was calculated from the median value (x_{med}) and standard deviation (p):

$$\sigma = p/x_{med} \tag{3}$$

To analyze the particle diameter distribution of STCA rods (Figure 3c), the conversion of pixels into micrometer units was applied to topological AFM images from Figure 3a by using the *SetScale* function in the ImageJ program. Then, the diameter of all rods in the image was measured manually, and the resulting values were used to build a histogram plot in the OriginPro 2018 program.[52] Finally, multiple peak fit was applied to the diameter distribution histograms using the Gaussian peak function, and the average diameter corresponding to the maximum value of the Gaussian function and its standard deviation were extracted.

To calculate the surface area of calixarene fibers, Gwyddion-processed AFM images of the STCA-containing surface were transformed into the grayscale color model and binarized, and the pixel-to-micrometer conversion was performed using the ImageJ software. Then, the calixarene fibers were segmented from the background by manual adjustment of the threshold value, and the total interstitial space area between calixarene fibers on different types of substrates was calculated using the Analyze particles tool. Finally, the total interstitial space area was subtracted from the total image area, and the surface area of calixarene fibers was calculated.

To perform fiber distribution analysis, a unique algorithm with the generation of Voronoi diagrams was developed, and Voronoi entropy was calculated using the Wolfram Mathematica version 13.3 program.[53] Voronoi entropy is a dimensionless measure of the orderliness of a set of points on a 2D plane so that $S_{Voronoi} = 0$ for an ideally ordered set and $S_{Voronoi} = 1.710$ for a random set.[40,54] More specifically, the color image was binarized through the binarizedImg function with the specification of the degree of binarization. Then, the image was segmented into morphological components of the background, and their centroids were determined. Using the *VoronoiMesh* function, a Voronoi network was generated based on these centroids. Application of the *Interior* function further excluded the outer layer of polygons at the image border from extracting the interior polygons. The *colorFunction* command was used to distinguish between polygons according to the number of their sides. Finally, the Voronoi entropy was calculated according to the following equation:

$$S_{Voronoi} = -\sum_{n} P_n \ln P_n \tag{4}$$

where P_n is the fraction of polygons with n sides.

DFT Calculations. The geometry of all model structures was optimized at the B3LYP-D3/def2-SVP level of theory using the Orca 5.0.4 program package.[55] The following convergence tolerance criteria were used: energy change 5.0×10^{-6} Eh, maximum gradient 3.0×10^{-4} Eh·b^{-1}, RMS gradient 1.0×10^{-4} Eh·b^{-1}, maximum displacement 4.0×10^{-3} b, and RMS displacement 2.0×10^{-3} b. The RIJCOSX approximation[56,57] utilizing the def2-SVP/C auxiliary basis sets, as well as spin-restricted approximation, was used to reduce the computational costs. The couple perturbed self-consistent field equations were solved by using the conjugated gradient method. The Hessian calculations were carried out numerically for neutral and anionic STCA monomers, STCA dimers, silanol network, PEI, and PEI-H^+ to determine the location of a minimum on the potential energy surfaces. In all model systems, there are no imaginary frequencies higher than -10 cm^{-1}, which are acceptable for large and conformationally flexible systems with more than 100 atoms.[58] The Gibbs free energies (G) of the model systems were estimated at 298.15 K and 1 atm. The thermodynamic favorability of STCA dimerization was evaluated by the difference of the binding energies of the STCA dimer and two STCA monomers in terms of Gibbs free energies (ΔG), whereas the association involving the silanol network was evaluated by the differences of corresponding total electronic energy values (ΔE) due to huge computational resources demands. The atoms of silanol network were constrained in the case of the Si−PEI system and three-component assemblies. The ChemCraft 1.8 program[59] was used for the visualization of model structures of monomers and associates. Cartesian atomic coordinates of all model structures are given in the Supporting Information as *xyz*-files.

■ ASSOCIATED CONTENT

Supporting Information

The Supporting Information is available free of charge at https://pubs.acs.org/doi/10.1021/acs.langmuir.4c03488.

AFM images of surfaces, approach force−distance curves with and without outliers, original set of stiffness and Young's modulus values, Voronoi tessellations of optical images for samples, and ^{1}H and ^{13}C NMR spectra of sulfonatothiacalix[4]arene (PDF)

Transformation of face-to-face and laterally oriented dimers of STCA into dimer **1** (MP4)

https://doi.org/10.1021/acs.langmuir.4c03488
Langmuir XXXX, XXX, XXX−XXX

Breaking of the intermolecular H-bond in the dimer with face-to-face oriented lower-rim OH groups (MP4)

AUTHOR INFORMATION

Corresponding Authors

Ekaterina V. Skorb − *Infochemistry Scientific Center, ITMO University, Saint Petersburg 191002, Russia;* orcid.org/0000-0003-0888-1693; Email: skorb@itmo.ru

Anton A. Muravev − *Infochemistry Scientific Center, ITMO University, Saint Petersburg 191002, Russia;* orcid.org/0000-0002-2245-3460; Email: muravev@itmo.ru

Authors

Anna A. Botnar − *Infochemistry Scientific Center, ITMO University, Saint Petersburg 191002, Russia*

Oleg P. Novikov − *Infochemistry Scientific Center, ITMO University, Saint Petersburg 191002, Russia*

Oleg A. Korepanov − *NT-MDT BV, Apeldoorn 7327, Netherlands*

Ekaterina A. Muraveva − *Infochemistry Scientific Center, ITMO University, Saint Petersburg 191002, Russia*

Dmitry A. Kozodaev − *NT-MDT BV, Apeldoorn 7327, Netherlands*

Alexander S. Novikov − *Infochemistry Scientific Center, ITMO University, Saint Petersburg 191002, Russia;* orcid.org/0000-0001-9913-5324

Michael Nosonovsky − *Infochemistry Scientific Center, ITMO University, Saint Petersburg 191002, Russia;* orcid.org/0000-0003-0980-3670

Complete contact information is available at: https://pubs.acs.org/10.1021/acs.langmuir.4c03488

Author Contributions

The manuscript was written through contributions of all authors. All authors have given approval to the final version of the manuscript. Anna A. Botnar: investigation, validation, formal analysis, writing−original draft; Oleg P. Novikov: software, formal analysis, writing−original draft; Oleg A. Korepanov: conceptualization, validation, writing−original draft; Ekaterina A. Muraveva: investigation, writing−original draft; Dmitry A. Kozodaev: conceptualization, writing−original draft; Alexander S. Novikov: conceptualization, writing−review and editing; Michael Nosonovsky: conceptualization, writing−review and editing; Ekaterina V. Skorb: resources, conceptualization, writing−review and editing; Anton A. Muravev: resources, project administration, conceptualization, supervision, writing−review and editing.

Notes

The authors declare no competing financial interest.

ACKNOWLEDGMENTS

The work was supported by the Russian Science Foundation (project no. 21-73-10185). The authors acknowledge the Priority 2030 Program for infrastructural support.

REFERENCES

(1) Xu, W.; Ledin, P. A.; Shevchenko, V. V.; Tsukruk, V. V. Architecture, Assembly, and Emerging Applications of Branched Functional Polyelectrolytes and Poly(Ionic Liquid)s. *ACS Appl. Mater. Interfaces* **2015**, *7*, 12570−12596.

(2) Seo, J. H.; Namdas, E. B.; Gutacker, A.; Heeger, A. J.; Bazan, G. C. Solution-Processed Organic Light-Emitting Transistors Incorporating Conjugated Polyelectrolytes. *Adv. Funct. Mater.* **2011**, *21*, 3667−3672.

(3) Soh, S.; Chen, X.; Vella, S. J.; Choi, W.; Gong, J.; Whitesides, G. M. Layer-by-Layer Films for Tunable and Rewritable Control of Contact Electrification. *Soft Matter* **2013**, *9*, 10233−10238.

(4) He, Y.; Cheng, Y.; Yang, C.; Guo, C. F. Creep-Free Polyelectrolyte Elastomer for Drift-Free Iontronic Sensing. *Nat. Mater.* **2024**, *23*, 1107.

(5) Yuan, Y.-M.; Liu, B.; Adibeig, M. R.; Xue, Q.; Qin, C.; Sun, Q.-Y.; Jin, Y.; Wang, M.; Yang, C.; Yuan, Y.-M.; Liu, B.; Adibeig, M. R.; Xue, Q.; Yang, C.; Qin, C.; Sun, Q.-Y.; Jin, Y.; Wang, M. Microstructured Polyelectrolyte Elastomer-Based Ionotronic Sensors with High Sensitivities and Excellent Stability for Artificial Skins. *Adv. Mater.* **2024**, *36*, No. 2310429.

(6) Baldina, A. A.; Pershina, L. V.; Noskova, U. V.; Nikitina, A. A.; Muravev, A. A.; Skorb, E. V.; Nikolaev, K. G. Uricase Crowding via Polyelectrolyte Layers Coacervation for Carbon Fiber-Based Electrochemical Detection of Uric Acid. *Polymers (Basel).* **2022**, *14*, 5145.

(7) Movilli, J.; Huskens, J. Functionalized Polyelectrolytes for Bioengineered Interfaces and Biosensing Applications. *Org. Mater.* **2020**, *2*, 78−107.

(8) Achazi, K.; Haag, R.; Ballauff, M.; Dernedde, J.; Kizhakkedathu, J. N.; Maysinger, D.; Multhaup, G. Understanding the Interaction of Polyelectrolyte Architectures with Proteins and Biosystems. *Angew. Chem., Int. Ed.* **2021**, *60*, 3882−3904.

(9) Cristofolini, L.; Szczepanowicz, K.; Orsi, D.; Rimoldi, T.; Albertini, F.; Warszynski, P. Hybrid Polyelectrolyte/Fe3O4 Nanocapsules for Hyperthermia Applications. *ACS Appl. Mater. Interfaces* **2016**, *8*, 25043−25050.

(10) Lama, N.; Wilhite, J.; Lvov, Y.; Konnova, S.; Fakhrullin, R. Clay Nanotube Coating on Cotton Fibers for Enhanced Flame-Retardancy and Antibacterial Properties. *ChemNanoMat* **2023**, *9*, No. e202300106.

(11) Borodina, T.; Yurina, D.; Sokovikov, A.; Karimov, D.; Bukreeva, T.; Khaydukov, E.; Shchukin, D. A Microwave-Triggered Opening of the Multifunctional Polyelectrolyte Capsules with Nanodiamonds in the Shell Composition. *Polymer (Guildf).* **2021**, *212*, No. 123299.

(12) Andreeva, D. V.; Trushin, M.; Nikitina, A.; Costa, M. C. F.; Cherepanov, P. V.; Holwill, M.; Chen, S.; Yang, K.; Chee, S. W.; Mirsaidov, U.; Castro Neto, A. H.; Novoselov, K. S. Two-Dimensional Adaptive Membranes with Programmable Water and Ionic Channels. *Nat. Nanotechnol.* **2021**, *16*, 174−180.

(13) Yuan, W.; Weng, G. M.; Lipton, J.; Li, C. M.; Van Tassel, P. R.; Taylor, A. D. Weak Polyelectrolyte-Based Multilayers via Layer-by-Layer Assembly: Approaches, Properties, and Applications. *Adv. Colloid Interface Sci.* **2020**, *282*, No. 102200.

(14) Li, J.; Parakhonskiy, B. V.; Skirtach, A. G. A Decade of Developing Applications Exploiting the Properties of Polyelectrolyte Multilayer Capsules. *Chem. Commun.* **2023**, *59*, 807−835.

(15) Tang, S.; Gong, J.; Shi, Y.; Wen, S.; Zhao, Q. Spontaneous Water-on-Water Spreading of Polyelectrolyte Membranes Inspired by Skin Formation. *Nat. Commun.* **2022**, *13*, 3227.

(16) Mateos-Maroto, A.; Abelenda-núñez, I.; Ortega, F.; Rubio, R. G.; Guzmán, E. Polyelectrolyte Multilayers on Soft Colloidal Nanosurfaces: A New Life for the Layer-By-Layer Method. *Polymers (Basel).* **2021**, *13*, 1221.

(17) Seddon, W. D.; Alfhaid, L.; Dunbar, A. D. F.; Geoghegan, M.; Williams, N. H. Adhesion of Grafted-to Polyelectrolyte Brushes Functionalized with Calix[4]Resorcinarene and Deposited as a Monolayer. *Langmuir* **2020**, *36*, 13843−13852.

(18) Motta, V.; Schäfer, M.; Hühn, J.; Zierold, R.; Blick, R. H.; Parak, W. J.; Weitzel, K.-M. Ion Selective Transport of Alkali Ions through a Polyelectrolyte Membrane. *Adv. Mater. Interfaces* **2020**, *7*, No. 2000419.

(19) Toutianoush, A.; Schnepf, J.; El Hashani, A.; Tieke, B. Selective Ion Transport and Complexation in Layer-by-Layer Assemblies of p-Sulfonato- Calix[n]Arenes and Cationic Polyelectrolytes. *Adv. Funct. Mater.* **2005**, *15*, 700−708.

(20) Basílio, N.; Piñeiro, Á.; Da Silva, J. P.; García-Río, L. Cooperative Assembly of Discrete Stacked Aggregates Driven by Supramolecular Host-Guest Complexation. *J. Org. Chem.* **2013**, *78*, 9113−9119.

(21) Fraix, A.; Afonso, D.; Consoli, G. M. L.; Sortino, S. A Calix[4]Arene-Based Ternary Supramolecular Nanoassembly with

Improved Fluoroquinolone Photostability and Enhanced NO Photorelease. *Photochem. Photobiol. Sci.* **2019**, *18*, 2216−2224.
(22) Crowley, P. B. Protein-Calixarene Complexation: From Recognition to Assembly. *Acc. Chem. Res.* **2022**, *55*, 2019−2032.
(23) Muravev, A. A.; Voloshina, A. D.; Sapunova, A. S.; Gabdrakhmanova, F. B.; Lenina, O. A.; Petrov, K. A.; Shityakov, S. V.; Skorb, E. V.; Solovieva, S. E.; Antipin, I. S. Calix[4]Arene−Pyrazole Conjugates as Potential Cancer Therapeutics. *Bioorg. Chem.* **2023**, *139*, No. 106742.
(24) Yamasaki, Y.; Shio, H.; Amimoto, T.; Sekiya, R.; Haino, T. Majority-Rules Effect and Allostery in Molecular Recognition of Calix[4]Arene-Based Triple-Stranded Metallohelicates. *Chem. − Eur. J.* **2018**, *24*, 8558−8568.
(25) Seganish, J. L.; Santacroce, P. V.; Salimian, K. J.; Fettinger, J. C.; Zavalij, P.; Davis, J. T. Regulating Supramolecular Function in Membranes: Calixarenes That Enable or Inhibit Transmembrane Cl− Transport. *Angew. Chem., Int. Ed.* **2006**, *45*, 3334−3338.
(26) Muravev, A.; Yakupov, A.; Gerasimova, T.; Nugmanov, R.; Trushina, E.; Babaeva, O.; Nizameeva, G.; Syakaev, V.; Katsyuba, S.; Selektor, S.; Solovieva, S.; Antipin, I. Switching Ion Binding Selectivity of Thiacalix[4]Arene Monocrowns at Liquid−Liquid and 2D-Confined Interfaces. *Int. J. Mol. Sci.* **2021**, *22*, 3535.
(27) Moradi, M.; Tulli, L. G.; Nowakowski, J.; Baljozovic, M.; Jung, T. A.; Shahgaldian, P. Two-Dimensional Calix[4]Arene-Based Metal−Organic Coordination Networks of Tunable Crystallinity. *Angew. Chem., Int. Ed.* **2017**, *56*, 14395−14399.
(28) Muravev, A.; Yakupov, A.; Gerasimova, T.; Islamov, D.; Lazarenko, V.; Shokurov, A.; Ovsyannikov, A.; Dorovatovskii, P.; Zubavichus, Y.; Naumkin, A.; Selektor, S.; Solovieva, S.; Antipin, I. Thiacalixarenes with Sulfur Functionalities at Lower Rim: Heavy Metal Ion Binding in Solution and 2D-Confined Space. *Int. J. Mol. Sci.* **2022**, *23*, 2341.
(29) De Izarra, A.; Park, S.; Lee, J.; Lansac, Y.; Jang, Y. H. Ionic Liquid Designed for PEDOT:PSS Conductivity Enhancement. *J. Am. Chem. Soc.* **2018**, *140*, 5375−5384.
(30) Zheng, S. Y.; Zhou, J.; Wang, S.; Wang, Y. J.; Liu, S.; Du, G.; Zhang, D.; Fu, J.; Lin, J.; Wu, Z. L.; Zheng, Q.; Yang, J. Water-Triggered Spontaneously Solidified Adhesive: From Instant and Strong Underwater Adhesion to In Situ Signal Transmission. *Adv. Funct. Mater.* **2022**, *32*, 2205597.
(31) Zeng, X.; Liu, Y.; Kang, Y.; Li, Q.; Xia, Y.; Zhu, Y.; Hou, H.; Uddin, M. H.; Gengenbach, T. R.; Xia, D.; Sun, C.; McCarthy, D. T.; Deletic, A.; Yu, J.; Zhang, X. Simultaneously Tuning Charge Separation and Oxygen Reduction Pathway on Graphitic Carbon Nitride by Polyethylenimine for Boosted Photocatalytic Hydrogen Peroxide Production. *ACS Catal.* **2020**, *10*, 3697−3706.
(32) Ye, E.; Chen, Z.; Shi, Y.; Zhang, D.; Li, W.; Qin, H.; Luo, Z.; Wu, Q.; Lin, Q.; Pan, H.; Wang, K. Self-Assembled Synthesis of Pd/SPEn from Polyelectrolyte Membranes for Efficient Direct Synthesis of H2O2 via Inhibiting the Dissociation of O − O Bond. *Chem. Eng. J.* **2023**, *472*, No. 144912.
(33) Chandrashekar, A.; Belardinelli, P.; Bessa, M. A.; Staufer, U.; Alijani, F. Quantifying Nanoscale Forces Using Machine Learning in Dynamic Atomic Force Microscopy. *Nanoscale Adv.* **2022**, *4*, 2134−2143.
(34) Belardinelli, P.; Chandrashekar, A.; Wiebe, R.; Alijani, F.; Lenci, S. Machine Learning to Probe Modal Interaction in Dynamic Atomic Force Microscopy. *Mech. Syst. Signal Process.* **2022**, *179*, No. 109312.
(35) Zhukov, M. V.; Aglikov, A. S.; Sabboukh, M.; Kozodaev, D. A.; Aliev, T. A.; Ulasevich, S. A.; Nosonovsky, M.; Skorb, E. V. AFM-Topological Data Analysis of Brass after Ultrasonic Surface Modification. *ACS Appl. Eng. Mater.* **2023**, *1*, 2084−2091.
(36) Pimpinelli, A.; Tumbek, L.; Winkler, A. Scaling and Exponent Equalities in Island Nucleation: Novel Results and Application to Organic Films. *J. Phys. Chem. Lett.* **2014**, *5*, 995−998.
(37) Gallops, C. E.; Yu, C.; Ziebarth, J. D.; Wang, Y. Effect of the Protonation Level and Ionic Strength on the Structure of Linear Polyethyleneimine. *ACS Omega* **2019**, *4*, 7255−7264.
(38) Karothu, D. P.; Halabi, J. M.; Ahmed, E.; Ferreira, R.; Spackman, P. R.; Spackman, M. A.; Naumov, P. Global Analysis of the Mechanical Properties of Organic Crystals. *Angew. Chem., Int. Ed.* **2022**, *61*, No. e202113988.
(39) Vanlandingham, M. R.; Mcknight, S. H.; Palmese, G. R.; Elings, J. R.; Huang, X.; Bogetti, T. A.; Eduljee, R. F.; Gillespie, J. W. Nanoscale Indentation of Polymer Systems Using the Atomic Force Microscope. *J. Adhes.* **1997**, *64*, 31−59.
(40) Bormashenko, E.; Frenkel, M.; Vilk, A.; Legchenkova, I.; Fedorets, A. A.; Aktaev, N. E.; Dombrovsky, L. A.; Nosonovsky, M. Characterization of Self-Assembled 2D Patterns with Voronoi Entropy. *Entropy* **2018**, *20*, 956.
(41) Limaye, A. V.; Narhe, R. D.; Dhote, A. M.; Ogale, S. B. Evidence for Convective Effects in Breath Figure Formation on Volatile Fluid Surfaces. *Phys. Rev. Lett.* **1996**, *76*, 3762.
(42) Yuan, D.; Zhu, W.-X.; Ma, S.; Yan, X. Bilayer Structure of Tetrasodium Thiacalix[4]arene Tetrasulfonate. *J. Mol. Struct.* **2002**, *616*, 241.
(43) De Sousa, S. M.; Fernandes, S. A.; De Almeida, W. B.; Guimarães, L.; Abranches, P. A.; Varejão, E. V.; Nascimento, C. S., Jr Theoretical Investigation on the Molecular Inclusion Process of Prilocaine into *p*-sulfonic Acid Calix[6]arene. *Chem. Phys. Lett.* **2016**, *646*, 52−55.
(44) Reis, S.; Liberto, N. A.; Fernandes, S. A.; de Fátima, A.; De Almeida, W. B.; Guimarães, L.; Nascimento, C. S., Jr Theoretical Investigation on the Molecular Inclusion Process of Urease Inhibitors into *p*-sulfonic Acid Calix[*4*,*6*]arenes. *Chem. Phys. Lett.* **2018**, *692*, 117−123.
(45) Xiong, K.; Jiang, F.; Wu, M.; Gai, Y.; Chen, Q.; Zhang, S.; Ma, J.; Han, D.; Hong, M. Two Novel Chains Based on Capsules Supported by Water-Soluble Calixarenes and Metal Complexes. *J. Solid State Chem.* **2012**, *192*, 215−220.
(46) Guo, Q. L.; Zhu, W. X.; Ma, S. L.; Yuan, D. Q.; Dong, S. J.; Xu, M. Q. Syntheses and Structural Characterization of Trivalent Lanthanide Complexes of *p*-Sulfonatothiacalix[4]Arene. *J. Mol. Struct.* **2004**, *690*, 63−68.
(47) Liu, Y.; Chen, K.; Guo, D. S.; Li, Q.; Song, H. B. Comparable Inclusion and Aggregation Structures of *p*-Sulfonatothiacalix [4] arene and *p*-Sulfonatocalix [4] arene upon Complexation with Quinoline Guests. *Cryst. Growth Des.* **2007**, *7*, 2601−2608.
(48) Iki, N.; Horiuchi, T.; Oka, H.; Koyama, K.; Morohashi, N.; Kabuto, C.; Miyano, S. Energy Transfer Luminescence of Tb^{3+} Ion Complexed with Calix[4]Arenetetrasulfonate and the Thia and Sulfonyl Analogue. The Effect of Bridging Groups. *J. Chem. Soc., Perkin Trans.* **2001**, *2* (11), 2219−2225.
(49) Nečas, D.; Klapetek, P.; *Gwyddion* − Free SPM (AFM, SNOM/NSOM, STM, MFM, ···) data analysis software. http://gwyddion.net.
(50) Roa, J. J.; Oncins, G.; Diaz, J.; Sanz, F.; Segarra, M. Calculation of Young's Modulus Value by Means of AFM. *Recent Pat. Nanotechnol.* **2011**, *5*, 27−36.
(51) Rasband, W. *ImageJ*. https://imagej.net/ij/.
(52) *Origin 2018*. https://www.originlab.com/2018.
(53) Wolfram, S. *Wolfram Mathematica: The world's definitive system for Modern Technical Computing*. https://www.wolfram.com/mathematica/index.php.en?source=footer.
(54) Shityakov, S.; Aglikov, A. S.; Skorb, E. V.; Nosonovsky, M. Voronoi Entropy as a Ligand Molecular Descriptor of Protein-Ligand Interactions. *ACS Omega* **2023**, *8*, 46190−46196.
(55) Neese, F.; Wiley, J. The ORCA Program System. *Wiley Interdiscip. Rev. Comput. Mol. Sci.* **2012**, *2*, 73−78.
(56) Neese, F.; Wennmohs, F.; Hansen, A.; Becker, U. Efficient, Approximate and Parallel Hartree−Fock and Hybrid DFT Calculations. A 'Chain-of-Spheres' Algorithm for the Hartree−Fock Exchange. *Chem. Phys.* **2009**, *356*, 98−109.
(57) Neese, F. An Improvement of the Resolution of the Identity Approximation for the Formation of the Coulomb Matrix. *J. Comput. Chem.* **2003**, *24*, 1740−1747.
(58) Bursch, M.; Mewes, J. M.; Hansen, A.; Grimme, S. Best-Practice DFT Protocols for Basic Molecular Computational Chemistry. *Angew. Chem., Int. Ed.* **2022**, *61*, No. e202205735.

https://doi.org/10.1021/acs.langmuir.4c03488
Langmuir XXXX, XXX, XXX−XXX

(59) Zhurko, G. A. *Chemcraft* - Graphical program for visualization of quantum chemistry computations. https://www.chemcraftprog.com.

https://doi.org/10.1021/acs.langmuir.4c03488
Langmuir XXXX, XXX, XXX−XXX